Analysis framework for nuclear heating effects on HTS-based conductors in fusion power plants

EUCAS23-3-LP-FM-06I

Analysis framework for nuclear heating effects on HTS-based conductors in fusion power plants

S. Sparacio, S. Viarengo, F. Ledda, D. Torsello, N. Riva, Z. S. Hartwig, L. Savoldi, and F. Laviano

***Abstract*—High-temperature superconducting-slotted cables, including the VIPER cable, are being investigated as possible candidates for winding the toroidal field coils of compact nuclear fusion machines, such as ARC. The higher performance of HTS materials in terms of magnetic fields and currents allows them to reduce their size compared to machines based on Nb alloys and compounds. However, compactness also means a closer interaction between the plasma products and the coils, creating new technological challenges to be faced. Among the others, the thermal effects induced on the superconducting materials by direct particles (i.e., neutrons), secondary particles and gamma-ray heating, will be stronger than for low-field larger machines and must be quantified. In this paper, a detailed thermo-magnetic model is built up using the software COMSOL Multiphysics® to simulate the consequences of the D-T plasma operation products on the first turn of a toroidal field coil of the ARC preliminary machine design. The irradiation-induced heat load on the (RE)$Ba_2Cu_3O_{7-\delta}$ tapes, computed via Monte Carlo simulations, is used as input for the thermal analysis of the VIPER cable. At the same time, a homogenized T-A formulation is developed for checking the performance reduction in the current/field operating conditions.**

***Index Terms*—ARC fusion reactor, thermo-magnetic modelling, irradiation-induced heat load, TSTC, VIPER cable**

I. INTRODUCTION

IN the quest for efficient and sustainable energy production, fusion reactors have emerged as a promising solution due to their potential to provide abundant clean energy [1]. However, realizing practical fusion devices requires overcoming various engineering challenges, including the development of advanced superconducting cables capable of withstanding the demanding operating conditions and the harsh environment in which they are placed [2].

Traditional low-temperature superconductors (LTS) have been employed in earlier reactor designs, but their limitations in terms of lower critical temperature (T_c) and critical magnetic fields have prompted the exploration of high-temperature superconducting (HTS) materials for next-generation compact fusion plants [3]. Among the emerging HTS-based cable technologies, the Cable-in-Conduit Conductors [4], the Cross-Conductor Cables [5], the Roebel Cables [6], and the Twisted Stacked-Tape Cables (TSTC) [7], have garnered significant attention due to their remarkable advantages in terms of electromagnetic and mechanical stability, reduced AC losses, and current sharing characteristics.

In particular, the VIPER cable [8]- which is a specific configuration of the TSTC HTS architecture - offers a space-saving whorled arrangement of multiple HTS strands that enables efficient distribution of current. This enhances the overall current-carrying capability and current sharing of the cable system, thereby reducing AC losses.

Despite their outstanding properties, HTS materials are not immune to performance degradation; key factors to examine in the fusion context are radiation damage, various heat loads, cyclic mechanical stresses/strains, magnetic self-field effects, and aging. To make things even worse, the reduced size of the emerging compact fusion machines, such as the ARC design proposed by MIT [9], limits their shielding capability, increasing the neutron flux on the HTS magnets [10].

In the past, extensive research has been conducted to investigate the impact of nuclear load on TF coils for both large [11], [12], [13], [14] and compact machines [15]. These studies have approached the issue from different perspectives, with most of the focus being on thermal-hydraulic analyses [16], [17] and design criteria [18], [19].

In this paper, we explore the potential performance degradation of high-field high-current materials due to irradiation-induced heating and electromagnetic self-field, during normal operation.

As far as the authors know, the present is a pioneering work accounting for the comprehensive local heat deposition retrieved by a full-3D Monte Carlo simulation considering both primary and secondary particles (i.e., protons and electrons), as well as the gamma-ray heating.

The developed procedure can be applied to any cable layout, neutron environment and heat source; in this work the VIPER

This work is partially supported by the Ministry of Education, Universities and Research through the "Programma Operativo Nazionale (PON) Ricerca e Innovazione 2014–2020", and through the National Recovery and Resilience Plan funded by the European Union-NextGenerationEU, by the European Cooperation in Science and Technology (COST) action CA19108: "High-Temperature Superconductivity for Accelerating the Energy Transition", by the Italian Ministry of Foreign Affairs and International Cooperation, grant number US23GR16, and by Eni S.p.A. N. Riva acknowledge support by Commonwealth Fusion Systems and PSFC MIT via RPP27.

Corresponding author: S. Sparacio (email: simone.sparacio@polito.it)

S. Sparacio (e-mail: simone.sparacio@polito.it), F. Ledda (e-mail: federico.ledda@polito.it), D. Torsello (e-mail: daniele.torsello@polito.it), and F. Laviano (e-mail: francesco.laviano@polito.it) are with Department of Applied Science and Technology, Politecnico di Torino, Torino 10129, Italy and Istituto Nazionale di Fisica Nucleare, Sezione di Torino, Torino 10125, Italy.

S. Viarengo (e-mail: sofia.viarengo@polito.it), and L. Savoldi (e-mail: laura.savoldi@polito.it) are with Department of Energy "Galileo Ferraris", Politecnico di Torino, Torino 10129, Italy.

Z. S. Hartwig (e-mail: hartwig@psfc.mit.edu), and N. Riva (e-mail: nicoriva@mit.edu) are with MIT Plasma Science and Fusion Center, 167 Albany St, Cambridge, MA 02139, United States of America.

layout, as proposed in [8], exposed to the neutron spectra coming from an ARC-like configuration is considered.

On the other hand, thermal loads arising from off-normal conditions, such as plasma disruption, can become dominant with respect to neutron irradiation – even if on much shorter time scales – but out of the scope of this work.

Section II provides an overview of the cable design and parameters; the same are used also for the neutronic analysis, which results are detailed in Appendix A. In section III the modeling framework is deeply discussed, while section IV highlights the main results of both the thermal and the electromagnetic simulation. Finally, Appendix B deals with the reliability of the simplified model comparing it with a detailed 2D analysis.

II. CABLE DESIGN AND PARAMETERS

The VIPER arrangement, as reported in Figure 1, is composed of a central stabilizer copper core, with a single circular cooling channel in the middle, and four helicoidal slots for arranging the stacks. Each strand comprises 40 parallelly stacked SuperPower Inc. tapes. The SCS4050 conductors are 4 mm wide and less than 0.1 mm thick. To obtain the highest electromagnetic performances, the strands are rotated by 90° with respect to each other (i.e., up/down stacks are placed horizontally, while left/right stacks are placed vertically). To provide, respectively, thermal and mechanical stability to the assembly an internal copper (Cu) and an external stainless-steel (SS) jacket are set in place. The cable is also twisted with a 20 cm pitch to reduce the electromagnetic interferences, enhance the current carrying capability, and mitigate the AC losses.

This simplified layout, together with a vacuum pressure impregnation (VPI) single solder process – which enables an integrated mechanical, electrical, and thermal connection among different regions of the cable – makes it suitable for applications with limited installation space, such as compact fusion reactors. Such a cable is, in fact, designed to achieve 25-75 kA in the high-field region (> 10 T).

However, further advancements are still needed to optimize the electromagnetic response under transport current and high operating temperatures, thereby unlocking their full potential for practical applications.

III. ASSUMPTIONS AND MODELLING FRAMEWORK

In the present work, each of the 40-tape HTS stacks is equivalently represented by an anisotropic bulk, with properly homogenized/rescaled properties, as described in the next paragraphs. This choice has been proved to be justifiable in terms of computational costs and results accuracy both for the thermal [20] and the electromagnetic [21] analysis.

Indeed, notwithstanding the different (RE)$Ba_2Cu_3O_{7-\delta}$ (REBCO, RE = rare earth) constituent materials properties, a first rough evaluation of the characteristic thermal diffusion timescale within each tape at 20 K led to a maximum value of about 10^{-5} s, much smaller than the seconds-lasting plasma pulse. As a result, on the long timescale, the temperature gradient within each tape approaches zero. This is verified in Appendix B.

Nonetheless, from the electromagnetic point of view, the T-A approach and its homogenized version differ by less than 1% [21]; being careful, though, that even in the *full-scale* model the fields cross-section profile of the various superconducting (SC) layers is convoluted in a 1D thin sheet. This approximation is not always straightforwardly admissible, for example when strong gradients along the thickness are present. Such cases should be addressed in future works.

The commercial software COMSOL Multiphysics® [22] was adopted for the numerical solution of the present task. Thermal and electromagnetic physics have been independently solved, and each model incorporates appropriate material properties, heat generation/temperature profile, and boundary conditions. Both the heat load and the temperature profiles were superimposed onto the cable operating conditions to evaluate their impact on the thermal and electromagnetic performance, respectively. Here, the heat load refers to the power extracted by the Monte Carlo simulation, while the temperature profile is

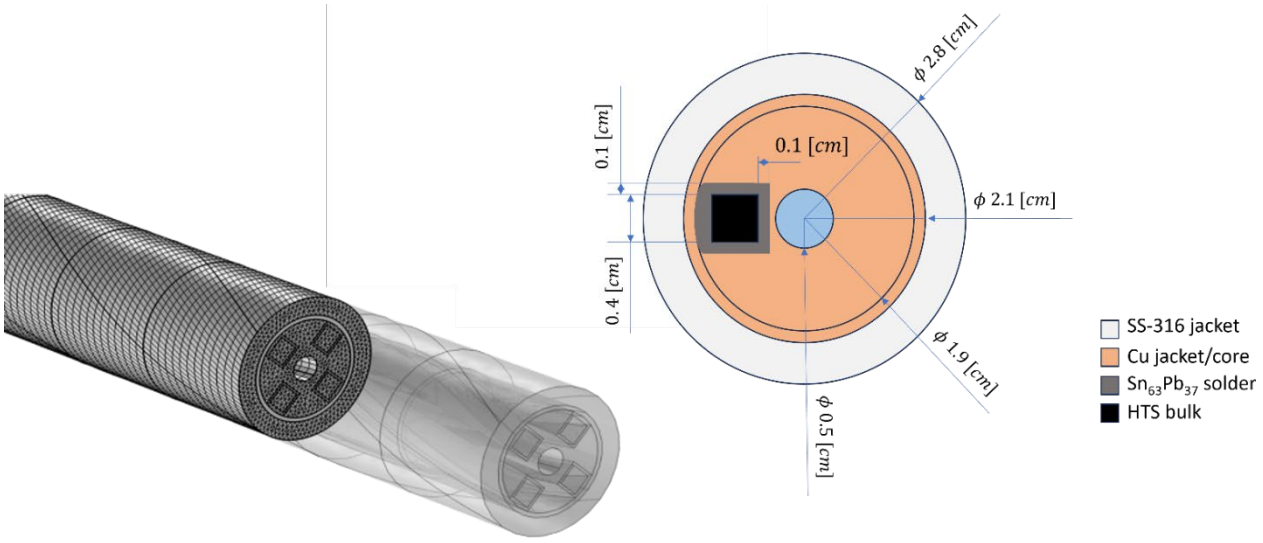

Fig. 1. Fully parametrized high-field VIPER cable. (Right) 2D sketch with the main quotes and color legend. (Left) 3D CAD and user-defined modelling mesh.

the one obtained by the thermal analysis and used as input in the electromagnetic part.

A. Thermal analysis

The thermal response of the cable is of paramount importance in assessing its performance. The radiation environment, especially in compact fusion reactors [10], can induce significant heat generation within the cable, leading to temperature gradients and potential degradation of the superconducting properties. Therefore, a comprehensive analysis is conducted to evaluate the cable capability to dissipate heat and maintain its SC characteristics.

Since the plasma pulse develops on a timescale much longer than any other cable thermal characteristic timescale, the following stationary governing equation has been considered:

$$-\nabla \cdot (k_i(\theta)\nabla\theta) = Q \tag{1}$$

where $k_i(\theta)\ [W/(m \cdot K)]$ is the temperature-dependent thermal conductivity of the i^{th} material, $\theta\ [K]$ is the temperature, and $Q\ [W/m^3]$ is the irradiation-induced thermal load (considering both neutrons and secondary particles) computed by Monte Carlo simulation [34], as described in Appendix A and reported in Fig. 2.

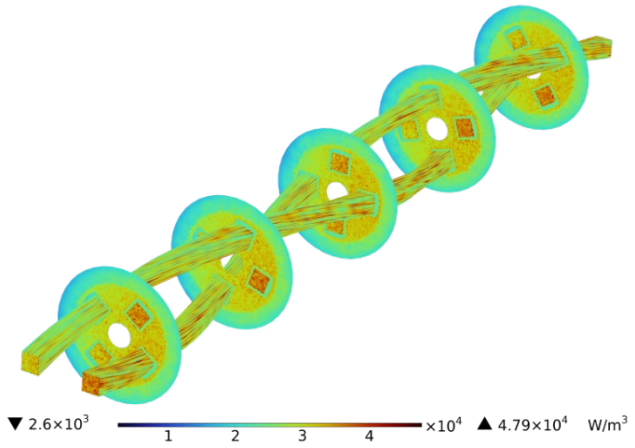

Fig. 2. Power density deposited within the cable because of the neutron flux of an ARC-like reactor at the inboard midplane of a toroidal field coil.

All the thermo-physical properties are temperature dependent and taken from [23], [24], [25], [26]. The homogenization approach of the HTS stacks follows the commonly used electrical analogy [27] and accounts for the tape microstructural anisotropy. While the effective mass density, ρ, and specific heat, C_p, are derived using an average weight for the tape cross-section.

The cable is treated as immersed in vacuum, meaning that the external surfaces are considered adiabatic. This choice results from having neglected the thick layer of insulation between the considered cable and its nearest neighbor, in the real winding pack design. As a result, the increased thermal diffusion time scale of the real cable structure makes the adiabatic condition a reasonable choice for the present research.

Exploiting the symmetry of the problem, a single cable pitch is simulated, and periodic boundary conditions are set on the lateral surfaces.

A steady state turbulent heat transfer coefficient [28]

$$h = 0.0259\left(\frac{k_{He}(\theta)}{D_h}\right) Re^{0.8} Pr^{0.4} \left(\frac{\theta}{\theta_{op}}\right)^{-0.716} \tag{2}$$

is imposed at the cooling channel interface emulating the convection process of 2 g/s supercritical helium at 10 bars. In Equation (2), $h\ [W/m^2 \cdot K]$ is the heat transfer coefficient towards supercritical helium, $D_h\ [m]$ is the hydraulic diameter (i.e., the cooling channel diameter in our case), $k_{He}(\theta)\ [W/m \cdot K]$ and $\theta_{op}\ [K]$ are the thermal conductivity and the bulk temperature of the supercritical helium, respectively; Re and Pr are the non-dimensional Reynolds and Prandtl numbers.

The governing contribution to the thermal propagation within the cable are, in the end, the thermal resistances between the different constituent materials. These resistances arise due to imperfect thermal coupling between layers of the cable and since realistic values may depend on the operating temperature, materials roughness, and contact pressures, their evaluation is intrinsically complex [29], [30]. In this work, a parametric study has been performed to determine the influence of all these factors on the thermal stability of the cable. An initial *mesh independence* analysis provided a relative difference of the order of 10^{-2} mK, guaranteeing a mK accuracy of the solution.

B. Electromagnetic analysis

Besides the thermal analysis, the electromagnetic behavior of the cable is of crucial importance in assessing its operating condition. In this work, the T-A homogenized formulation is employed, which enables a simplified analysis by homogenizing the complex structure of the tapes. For a detailed description of the T-A formulation, the reader is referred to [21]; here, we briefly recall the main aspects of the considered approach [31].

Within the framework of finite element method (FEM), this numerical technique couples the current vector potential **T** (exclusively defined over the SC layer) and the magnetic vector potential **A** (defined over the entire domain) through Ampere (3) and Faraday (4) law, as follow:

$$\nabla \times \left(\frac{1}{\mu}\nabla \times \boldsymbol{A}\right) = \boldsymbol{J} \tag{3}$$

$$\nabla \times (\rho \nabla \times \boldsymbol{T}) = -\frac{\partial \boldsymbol{B}}{\partial t} \tag{4}$$

where $\nabla \times \boldsymbol{A} = \boldsymbol{B}$ and $\nabla \times \boldsymbol{T} = \boldsymbol{J}$.

Here, $\boldsymbol{B} = [B_x, B_y, 0]$ and $\boldsymbol{J} = [0, 0, J_z]$ are the magnetic flux density and the current density, respectively.

The latter is assumed to circulate only within the superconducting domain – which, in this case, is a homogenized anisotropic SC bulk instead of a densely packed arrangement of tapes (see Fig. 3) – while the remaining part is considered non-conducting. μ is the permeability of vacuum and ρ is the electrical resistivity in the superconducting region.

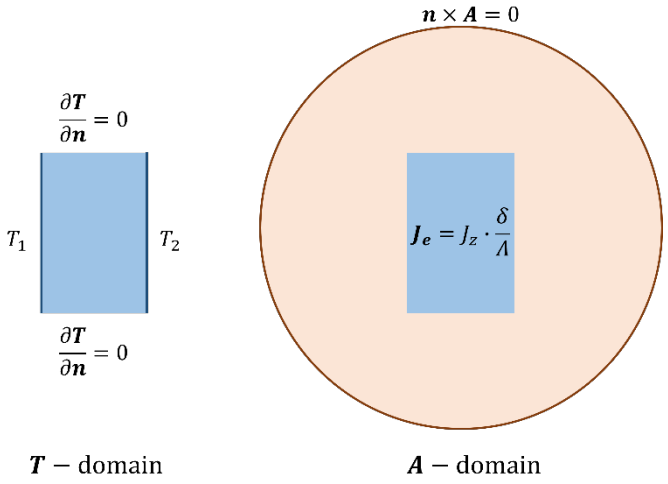

Fig. 3. T-A homogenization steps and boundary conditions as shown in [21]. The multilayer composite arrangement is condensed into a homogeneous bulk.

The coupling term (5) is expressed by an effective external current density within the A-domain (schematized in the right-hand side of Fig. 3), which will lead to the definition of the field strength vectors (H_1 and H_2) just above and below the superconductor.

$$\boldsymbol{n} \times (H_1 - H_2) = \boldsymbol{J} \cdot \frac{\delta}{\Lambda} \tag{5}$$

Here δ and Λ are, respectively, the thickness of the SC layer and the thickness of the whole tape. Their ratio rescales the current density flow within the bulk (as obtained from the model) as if it were flowing only within a fraction of it (i.e., the SC film), as physically expected.

The boundary conditions are related to the vector A, whether any external magnetic field or magnetic insulation is imposed at the boundary of the considered universe (brown circle in the right-hand side of Fig. 3), and to the vector T – as the integral of the current density J over the cross-sections of the tapes – at the lateral surfaces of the homogenized domain (schematized in the left-hand side of Fig. 3). The latter, being always perpendicular to the SC layer, takes the following expressions (6):

$$I = (T_1 - T_2)\delta \tag{6}$$

$$\frac{\partial \boldsymbol{T}}{\partial \boldsymbol{n}} = 0 \tag{7}$$

Where, depending on the tapes arrangement, T_1 and T_2 are the imposed potential at the periphery of the strips/bulk, as indicated by the blue vertical lines of Fig. 3, and (7) avoid spurious currents outside the SC domain.

The material response to external stimuli is provided by the widely used power law relationship (8).

$$\frac{\boldsymbol{E}}{E_c} = \left(\frac{\boldsymbol{J}}{J_c(B,\theta)}\right)^n \tag{8}$$

Here $E = [0, 0, E_z]$ is the electric field, $E_c = 1\ \mu V/cm$ is the critical electric field for determining the critical current density by the voltage criterion, and n is the creep exponent.

The critical current density J_c is defined by the following parametrized fitting curve (9), as reported in [27].

$$J_c(B,\theta) = \frac{D \cdot B_{irr0}^{\beta}}{B + \varepsilon B_0} \cdot f(t)^{\beta} \cdot \left[\frac{b}{f(t)}\right]^p \cdot \left[1 - \frac{b}{f(t)}\right]^q$$
$$f(t) = (1-t)^{\alpha}; \quad t = \frac{\theta}{\theta_{c0}}; \quad b = \frac{B + \varepsilon B_0}{B_{irr0}} \tag{9}$$

This experimentally obtained function is both field- and temperature-dependent and all the parameters inside are listed in Table I.

TABLE I
FITTING PARAMETERS [27] DEFINED IN (9)

NAME	UNIT	VALUE
D	[N/(m^{3}T$^{\beta}$)]	5.2254×10^8
Θ_{c0}	[K]	92
B_{irr0}	[T]	132.5
B_0	[T]	1.0
p	[-]	0.653
q	[-]	2.568
α	[-]	1.5
β	[-]	1.789
ε	[-]	0.0168

C. Geometrical considerations

The anisotropic nature and the helical pattern of REBCO require the adoption of general Curvilinear Coordinates accounting for the thermal properties' modifications, particularly the thermal conductivity, and the current-potential direction, through the twisting. It is noteworthy that in the considered cable design the left/right stacks are 90°-tilted with respect to the up/down ones (or vice versa), meaning that the current vector potential, $\boldsymbol{T}$, and the transversal thermal conductivity, k_T, have both two perpendicular components: T_y ($k_{T,y}$) for the up/down stacks and T_x ($k_{T,x}$) for the left/right stacks. Of course, x and y have meaning only in the Cartesian Coordinate System. In the new frame of reference, they must be projected on the new corresponding unit base vector (i.e., e_1 (blue) and e_2 (green), respectively); while e_3 (red) is referred to the z-direction, similarly to how it was done in [32].

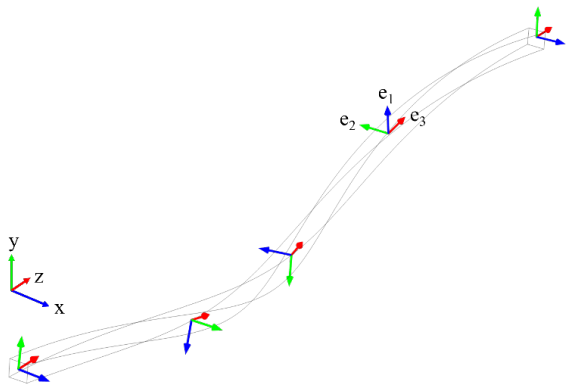

Fig. 4. General Curvilinear Coordinates sketch on one of the four modeled stacks, highlighting the original cartesian frame of reference (x, y, z) and the new one (e_1, e_2, e_3).

IV. RESULTS AND DISCUSSION

Fig. 2 highlights the necessity of a very material- and geometry-detailed analysis of the irradiation-induced heat load. The non-homogeneous power deposition within the cable builds up because of the different scattering cross-sections and cable position. Moreover, the presence of Ni within the Hastelloy substrate (about 50 wt% in the material) – which contributes to the (n, 2n) neutron multiplication within the SC tape - makes the most delicate component of the cable also the most affected in terms of deposited power. This, together with the large REBCO anisotropy and the presence of thermal contact resistances, suggests a further possible complication in the thermal stability of the cable.

Despite the uneven heat source distribution, the analysis revealed that the peak thermal conductivities at ~20 K, the VPI solder to maximize surface contact, and the central helium cooling in close proximity to all parts of the cable, result in a low-temperature rise and a quite homogeneous temperature map within each cable component; even perpendicularly to the tape thickness, where the thermal conductivity is largely unfavored (see Fig. 5).

These results corroborate what has been earlier proposed for the VIPER cable [3], [8] which provides an excellent capability to remove large amounts of nuclear heating without temperature rise or worrying gradients.

It must be pointed out, however, that having considered a single cable only, the backscattered particle contribution coming from the nearest neighbors' ones has not been considered, underestimating the deposited power at the upper, lower, and lateral (i.e., the side opposite to the neutron source) cable section. Moreover, because of the homogenization procedure, the thermal conductivity of the anisotropic bulk is orders of magnitude higher than the REBCO one and no inter-tape resistance has been accounted for. This, again, results in an underestimation of the maximum temperature and the relative gradients within the tapes.

On the other hand, the inclusion of thermal contact resistances allows a more realistic performance prediction of the HTS-based system, especially in the presence of interfaces between different materials. In this case, the temperature response depends on where these resistances arise, as well as their magnitudes.

In Fig. 6 a)-c), an insight look on the most sensitive component is presented for three different cases (i.e., 0, 5×10^{-4}, and 5×10^{-3} m^2K/W thermal contact resistance around the homogenized bulk). The temperature gradients within the simplified composites change profile manifesting the maximum temperature in the middle of the bulks (see Fig. 6 b and c). The temperature gradients span two orders of magnitude, for an order of magnitude change in the interface thermal conductivity; despite this, the overall temperature increment still remains not appreciable concerning the operating temperature. This confirms the possibility of modelling the cable through successive simplifications (e.g., 0D object in the radial direction – considering the cable cross-section with its own homogeneous temperature – and 1D object in the axial direction), as already tackled by other authors for different scenarios [20], [32].

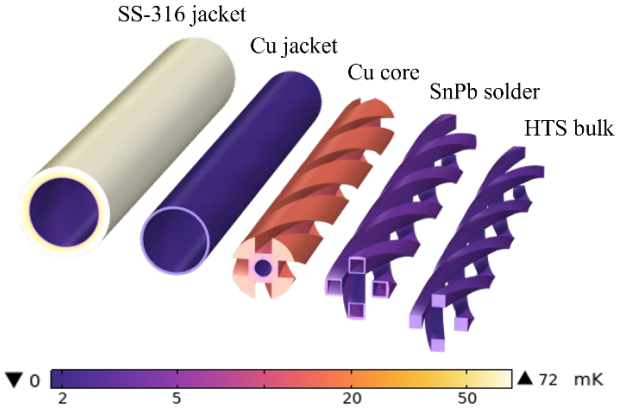

Fig. 5. Temperature increment with respect to the mean wetted surface temperature ($T_{mean,ws}$ = 20.606 K) of each cable component, in the case of no thermal contact resistance, on a log scale color legend for underlying the internal gradients.

From the electromagnetic point of view, instead, it is crucial to evaluate whether any evident degradation of the cable performance develops because of the temperature increment and how the current density profile changes because of the internal gradients. This has been done by a two-step parametric analysis: in the first step, the electromagnetic response has been evaluated at a fixed temperature of 20 K (the expected operating condition); in the second step, we have introduced the "non-homogeneous temperature map" obtained by the thermal analysis. The latter changes the local critical current density, changing the magnetic field penetration within the stacks, and changing again the critical current density.

In both steps, a 25 kA (i.e., around $0.5J_c$ at 20 K and 10 T) current is equally forced through the 160 tapes.

Fig. 7 shows the relative difference between the current density profile evaluated by the parametric sweep. This is strongly non-uniform and related to the cable twisting, SC arrangement, and the non-uniform temperature distribution.

No evident degradation of the electromagnetic performance, along the considered pitch, is observed because of the temperature increment, while a small difference in the current density profile is revealed because of the temperature gradients:

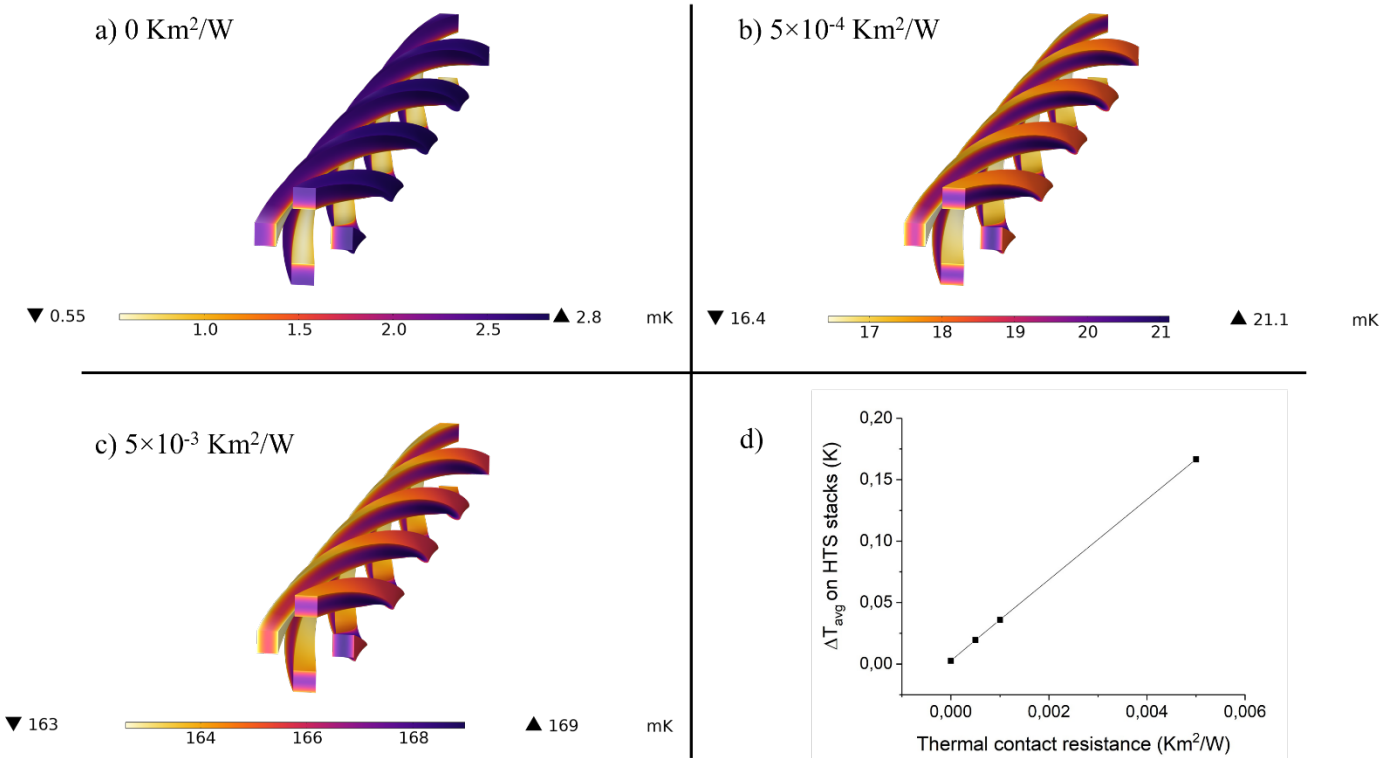

Fig. 6. Temperature increment with respect to the mean wetted surface temperature ($T_{mean,ws}$ = 20.606 K) of the four HTS-bulks in three different cases: a) no thermal contact resistance, b)-c) respectively 5×10^{-4} and 5×10^{-3} K m^2/W contact resistance around the homogenized bulks, d) average temperature increment trend with respect the resistance magnitude.

reduced critical current density close to the external surfaces results in a reduced current capability there, and a higher magnetic field penetration, while in the middle no significant difference between the two cases is developed.

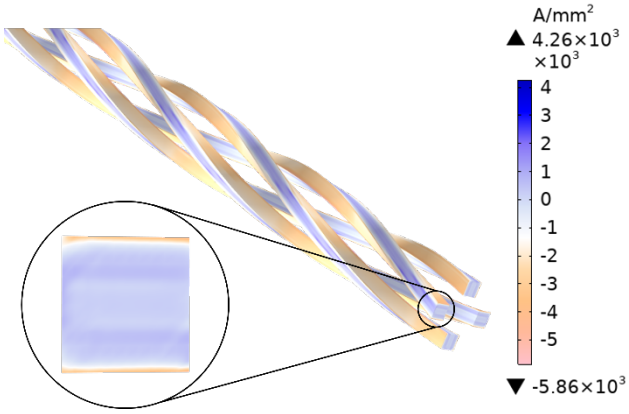

Fig. 7. Relative difference between the current density profile evaluated at the temperature obtained from the thermal analysis and the one at 20 K. The 3D map (right) and the 2D detail (bottom-left) show a very small variation due to the temperature increment.

V. Conclusion and Perspective

By considering the interplay between electromagnetic and thermal phenomena, the present analysis provides a thorough assessment of the cable performance, and its ability to withstand challenging conditions in an irradiation-prone environment. The negligible temperature increment resulting from the normal operation of a compact fusion machine confirms the design choices and the possibility of successive modelling simplification. Despite these results originate from a homogenization technique, which did not allow to consider the thermal contact resistance between tapes, the proper material distribution of the tapes (both from the Monte Carlo point of view and the thermo-magnetic one), the proper thermo-physical properties of the tapes, and the appropriate current density/magnetic flux profile within each superconducting layer, no serious changes are expected in the full-scale approach.

These conclusions are, nevertheless, well-founded only for the local stationary behavior of the considered machine. Different scenarios may require different considerations and it is important to carefully assess whether the benefits of simplification outweigh the potential loss of accuracy in specific applications. In this regard, extending the analysis to include the effect of insulation between cables and the winding pack is of huge interest for getting the behavior right for a large magnet, where the insulation will be the most critical thermal barrier.

Finally, a complementary analysis could contemplate the accumulations of the deposited heat over the length of the cable; even a relatively small amount of heat power can significantly add up with increasing cable length and possibly make the dissipation mechanisms ineffective. A verification of this would require a computational thermal fluid dynamic analysis accounting for the temperature increment of the supercritical helium subjected to 15.5 W/m irradiation load, along the nearly 25 m length of every individual CICC cable.

APPENDIX A

Together with the structural damage and material activation, the irradiation-induced thermal load on the coil system is of crucial importance in their performance characterization. In this frame, the neutron environment (i.e., neutron flux distribution and spectra) at the inboard midplane of a toroidal field magnet has been evaluated via a Monte Carlo simulation with the PHITS code and considering a 3D CAD model of the inner part of an ARC-like reactor and a neutron source respecting all plasma parameters [35]. It is worth mentioning that the neutron source coming from the deuterium-tritium reaction (reported in (10)) has, for a 525 MW fusion power machine, an emission intensity of about 1.8×10^{20} n/s.

$$D + T \rightarrow \alpha\ (3.5\ MeV) + n\ (14.1\ MeV) \qquad (10)$$

The so-obtained neutron spectrum is used as a source for a second 3D Monte Carlo simulation of a VIPER cable, where all the secondary particles are transported, yielding the deposited energy distribution over the whole cable. Considering both neutrons and secondary particles (including photons) it is fundamental to accurately describe the nuclear reaction mechanisms within the reactor components. Figure 9 and Figure 10 show, respectively, the neutrons and secondary particles flux, at both the inboard midplane of a toroidal field coil (blue line) and on the superconducting stacks (red line).

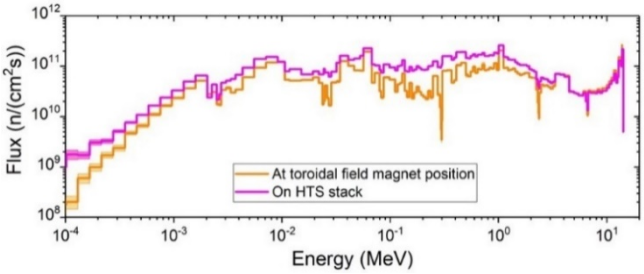

Fig. 8. Neutron spectrum at the toroidal field magnet position (inboard midplane) and on the HTS stack. The higher flux on the superconductors, over the whole energy range, is due to the multiplicative nature (n, 2n) of Nickel.

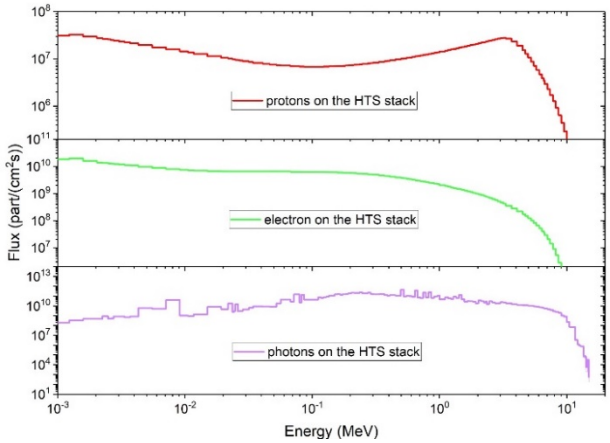

Fig. 9. Secondary particles and gamma-ray spectra on the HTS stack. Among them, electrons and photons have the highest flux.

The choice to perform the Monte Carlo simulations in two steps is imposed by the complexity and extreme duration of a complete 3D simulation of the whole reactor down to the single cable detail. This approach allowed to reduce the statistical error down to less than 15 %.

APPENDIX B

This section provides a simulation-based validation study aimed at assessing the reliability of the simplified computational model designed previously. The homogenized approach offers computational efficiency while retaining key aspects of the complex phenomena but some features (such as the right constituent materials properties distribution and the thermal contact resistances between different layers) cannot be considered.

In the absence of thermal inhomogeneity along the cable helix, a simple but detailed 2D thermal analysis is built up considering one cable cross-section (z = 0).

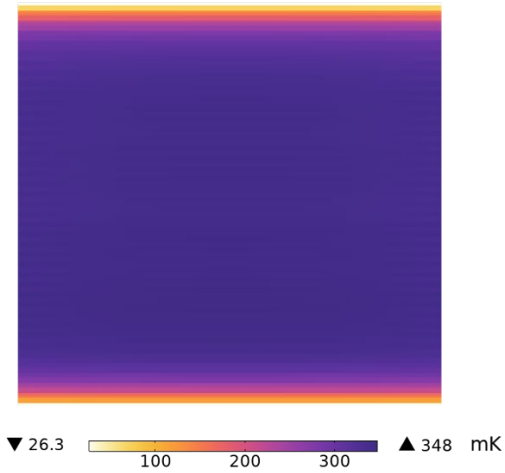

Fig. 10. Temperature distribution on the central-upper stack with 5×10^{-3} Km^2/W contact resistance between all the layer interfaces. The temperature is higher and more homogenous in the central part, while steeper gradients arise at the upper and bottom periphery of the stack. Despite these differences, no dangerous peak is reached.

In this case, we were able to include thermal contact resistance at the interface of each layer. Figure 10 shows the temperature profile of the central-upper stack with 5×10^{-3} Km^2/W contact resistance. The simulation results, which do not show strong gradients between each tape in the stack, validate the predictions of the simplified model across all test cases and confirm its applicability in the long-term scenario. The deviation between the two is also due to the different power distribution along the cable length: in the 2D case, the in-plane heat load is indefinitely repeated in the z-direction (being the cross-section on the x-y plane), while in the 3D case, each stack spans over the entire wire diameter and faces different heat loads. Moreover, using the right material distribution and properties makes the gradients steeper, as predicted, but still with no concern on the superconducting performance (the maximum temperature increment is less than 1 K).

REFERENCE

[1] S. Meschini *et al.*, "Review of commercial nuclear fusion projects," *Front. Energy Res.*, vol. 11, p. 1157394, Jun. 2023, doi: 10.3389/fenrg.2023.1157394.

[2] C. Barth, "High Temperature Superconductor Cable Concepts for Fusion Magnets".

[3] B. N. Sorbom *et al.*, "ARC: A compact, high-field, fusion nuclear science facility and demonstration power plant with demountable magnets," *Fusion Eng. Des.*, vol. 100, pp. 378–405, Nov. 2015, doi: 10.1016/j.fusengdes.2015.07.008.

[4] L. Muzzi, G. De Marzi, A. Di Zenobio, and A. Della Corte, "Cable-in-conduit conductors: lessons from the recent past for future developments with low and high temperature superconductors," *Supercond. Sci. Technol.*, vol. 28, no. 5, p. 053001, May 2015, doi: 10.1088/0953-2048/28/5/053001.

[5] M. J. Wolf, W. H. Fietz, C. M. Bayer, S. I. Schlachter, R. Heller, and K.-P. Weiss, "HTS CroCo: A Stacked HTS Conductor Optimized for High Currents and Long-Length Production," *IEEE Trans. Appl. Supercond.*, vol. 26, no. 2, pp. 19–24, Mar. 2016, doi: 10.1109/TASC.2016.2521323.

[6] W. Goldacker, F. Grilli, E. Pardo, A. Kario, S. I. Schlachter, and M. Vojenčiak, "Roebel cables from REBCO coated conductors: a one-century-old concept for the superconductivity of the future," *Supercond. Sci. Technol.*, vol. 27, no. 9, p. 093001, Sep. 2014, doi: 10.1088/0953-2048/27/9/093001.

[7] M. Takayasu, J. V. Minervini, and L. Bromberg, "HTS Twisted Stacked-Tape Cable Development".

[8] Z. S. Hartwig *et al.*, "VIPER: an industrially scalable high-current high-temperature superconductor cable," *Supercond. Sci. Technol.*, vol. 33, no. 11, p. 11LT01, Nov. 2020, doi: 10.1088/1361-6668/abb8c0.

[9] B. N. Sorbom *et al.*, "ARC: A compact, high-field, fusion nuclear science facility and demonstration power plant with demountable magnets," *Fusion Eng. Des.*, vol. 100, pp. 378–405, Nov. 2015, doi: 10.1016/j.fusengdes.2015.07.008.

[10] D. Torsello, D. Gambino, L. Gozzelino, A. Trotta, and F. Laviano, "Expected radiation environment and damage for YBCO tapes in compact fusion reactors," *Supercond. Sci. Technol.*, vol. 36, no. 1, p. 014003, Jan. 2023, doi: 10.1088/1361-6668/aca369.

[11] D. Bessette, E. Zapretilina, and N. Shatil, "Nuclear heat, disruption loads and other AC losses and their impact on the ITER toroidal field coils conductor design," *IEEE Trans. Appiled Supercond.*, vol. 10, no. 1, pp. 1074–1077, Mar. 2000, doi: 10.1109/77.828418.

[12] D. Bessette, N. Shatil, and E. Zapretilina, "Simulations of the ITER Toroidal Field Coil Operation With the VINCENTA Code," *IEEE Trans. Appl. Supercond.*, vol. 16, no. 2, pp. 795–798, Jun. 2006, doi: 10.1109/TASC.2006.873258.

[13] F. Cau, R. Forte, and A. Portone, "Modeling of ITER TF cooling system through 2D thermal analyses and enthalpy balance," *Fusion Eng. Des.*, vol. 124, pp. 18–23, Nov. 2017, doi: 10.1016/j.fusengdes.2017.06.036.

[14] D. V. Portnov, Yu. G. Vysokikh, Yu. A. Kashchuk, and R. N. Rodionov, "Tokamak with Reactor Technologies (TRT): Preliminary Analysis of Nuclear Energy Release in Toroidal Field Coils," *Plasma Phys. Rep.*, vol. 47, no. 12, pp. 1285–1290, Dec. 2021, doi: 10.1134/S1063780X21110234.

[15] B. Hamilton, "Analysis of Cryogenic Cooling of Toroidal Field Magnets for Nuclear Fusion Reactors".

[16] M. Lewandowska, A. Dembkowska, R. Heller, and M. Wolf, "Thermal-hydraulic analysis of an HTS DEMO TF coil," *Cryogenics*, vol. 96, pp. 125–132, Dec. 2018, doi: 10.1016/j.cryogenics.2018.10.014.

[17] R. Bonifetto, A. D. Zenobio, L. Muzzi, S. Turtu, R. Zanino, and A. Zappatore, "Thermal-Hydraulic Analysis of the DTT Toroidal Field Magnets in DC Operation," *IEEE Trans. Appl. Supercond.*, vol. 30, no. 4, pp. 1–5, Jun. 2020, doi: 10.1109/TASC.2020.2964517.

[18] G. M. Voss, A. Bond, J. E. G. Edwards, and T. C. Hender, "Toroidal field coil design for the spherical tokamak power plant," *Fusion Eng. Des.*, vol. 48, no. 3–4, pp. 407–418, Sep. 2000, doi: 10.1016/S0920-3796(00)00151-4.

[19] R. Heller, P. V. Gade, W. H. Fietz, T. Vogel, and K.-P. Weiss, "Conceptual Design Improvement of a Toroidal Field Coil for EU DEMO Using High-Temperature Superconductors," *IEEE Trans. Appl. Supercond.*, vol. 26, no. 4, pp. 1–5, Jun. 2016, doi: 10.1109/TASC.2016.2520662.

[20] A. Zappatore, W. H. Fietz, R. Heller, L. Savoldi, M. J. Wolf, and R. Zanino, "A critical assessment of thermal–hydraulic modeling of HTS twisted-stacked-tape cable conductors for fusion applications," *Supercond. Sci. Technol.*, vol. 32, no. 8, p. 084004, Aug. 2019, doi: 10.1088/1361-6668/ab20a9.

[21] F. Huber, W. Song, M. Zhang, and F. Grilli, "The T-A formulation: an efficient approach to model the macroscopic electromagnetic behaviour of HTS coated conductor applications," *Supercond. Sci. Technol.*, vol. 35, no. 4, p. 043003, Apr. 2022, doi: 10.1088/1361-6668/ac5163.

[22] "COMSOL: Multiphysics Software for Optimizing Designs," COMSOL. Accessed: Jul. 05, 2023. [Online]. Available: https://www.comsol.com/

[23] H. Fujishiro, M. Ikebe, T. Naito, K. Noto, S. Kohayashi, and S. Yoshizawa, "Anisotropic Thermal Diffusivity and Conductivity of YBCO(123) and YBCO(211) Mixed Crystals. I," *Jpn. J. Appl. Phys.*, vol. 33, no. 9R, p. 4965, Sep. 1994, doi: 10.1143/JJAP.33.4965.

[24] Y. Iwasa and K. R. Marken, "*Case Studies in Superconducting Magnets: Design and Operational Issues*," *Phys. Today*, vol. 48, no. 10, pp. 68–68, Oct. 1995, doi: 10.1063/1.2808214.

[25] N. Bagrets, C. Barth, and K.-P. Weiss, "Low Temperature Thermal and Thermo-Mechanical Properties of Soft Solders for Superconducting Applications," *IEEE Trans. Appl. Supercond.*, vol. 24, no. 3, pp. 1–3, Jun. 2014, doi: 10.1109/TASC.2013.2283869.

[26] "Thermophysical Properties of Fluid Systems." Accessed: Aug. 07, 2023. [Online]. Available: https://webbook.nist.gov/chemistry/fluid/

[27] M. Casali, M. Breschi, and P. L. Ribani, "Two-Dimensional Anisotropic Model of YBCO Coated Conductors," *IEEE Trans. Appl. Supercond.*, vol. 25, no. 1, pp. 1–12, Feb. 2015, doi: 10.1109/TASC.2014.2341180.

[28] P. J. Giarratano, V. D. Arp, and R. V. Smith, "Forced convection heat transfer to supercritical helium," 1971.

[29] P. G. Siddappa and A. Tariq, "Experimental estimation of thermal contact conductance across pressed copper–copper contacts at cryogenic-temperatures," *Appl. Therm. Eng.*, vol. 219, p. 119412, Jan. 2023, doi: 10.1016/j.applthermaleng.2022.119412.

[30] H. Fujishiro, T. Okamoto, and K. Hirose, "Thermal contact resistance between high-Tc superconductor and copper," *Phys. C Supercond.*, vol. 357–360, pp. 785–788, Sep. 2001, doi: 10.1016/S0921-4534(01)00364-1.

[31] C. R. Vargas-Llanos, F. Huber, N. Riva, M. Zhang, and F. Grilli, "3D homogenization of the T-A formulation for the analysis of coils with complex geometries." arXiv, Jun. 27, 2022. Accessed: Jul. 05, 2023. [Online]. Available: http://arxiv.org/abs/2206.09718

[32] N. Riva *et al.*, "Development of the first non-planar REBCO stellarator coil using VIPER cable," *Supercond. Sci. Technol.*, vol. 36, no. 10, p. 105001, Oct. 2023, doi: 10.1088/1361-6668/aced9d.

[33] Z. S. Hartwig *et al.*, "VIPER: an industrially scalable high-current high-temperature superconductor cable," *Supercond. Sci. Technol.*, vol. 33, no. 11, p. 11LT01, Nov. 2020, doi: 10.1088/1361-6668/abb8c0.

[34] F. Ledda, D. Torsello, D. Pettinari, S. Sparacio, Z. Hartwig, M. Zucchetti, and F. Laviano, "3D neutronic and secondary particles analysis on YBCO tapes for compact fusion reactors", *IEEE Trans. Appl. Supercond*., submitted.